Nano Research 2017, 10(9): 3189–3201
DOI 10.1007/s12274-017-1536-0
Research Article
ISSN 1998-0124
CN 11-5974/O4

Hierarchical Sb-Ni nanoarrays as robust binder-free anodes for high-performance sodium-ion half and full cells

Liying Liang[1], Yang Xu[1], Liaoyong Wen[1], Yueliang Li[2], Min Zhou[1], Chengliang Wang[1], Huaping Zhao[1], Ute Kaiser[2], and Yong Lei[1] (✉)

[1] *Institute of Physics & IMN MacroNano (ZIK), Ilmenau University of Technology, Professor Schmidt Strasse 26, 98693 Ilmenau, Germany*
[2] *Central Facility for Electron Microscopy, Electron Microscopy Group of Materials Science, Ulm University, Albert-Einstein-Allee 11, 89081 Ulm, Germany*

Received: 28 November 2016
Revised: 10 February 2017
Accepted: 13 February 2017

KEYWORDS
hierarchical Sb-Ni nanoarrays,
binder-free anode,
capacitive charge storage,
Na-ion full cell

ABSTRACT

A novel hierarchical electrode material for Na-ion batteries composed of Sb nanoplates on Ni nanorod arrays is developed to tackle the issues of the rapid capacity fading and poor rate capability of Sb-based materials. The three-dimensional (3D) Sb-Ni nanoarrays as anodes exhibit the synergistic effects of the two-dimensional nanoplates and the open and conductive array structure as well as strong structural integrity. Further, their capacitive behavior is confirmed through a kinetics analysis, which shows that their excellent Na-storage performance is attributable to their unique nanostructure. When used as binder-free sodium-ion battery (SIB) anodes, the nanoarrays exhibit a high capacity retention rate (more than 80% over 200 cycles) at a current density of 0.5 $A \cdot g^{-1}$ and excellent rate capacity (up to 20 $A \cdot g^{-1}$), with their capacity being 580 $mAh \cdot g^{-1}$. Moreover, a P2-$Na_{2/3}Ni_{1/3}Mn_{2/3}O_2$//3D Sb-Ni nanoarrays full cell delivers a highly reversible capacity of 579.8 $mAh \cdot g^{-1}$ over 200 cycles and an energy density as high as 100 $Wh \cdot kg^{-1}$. This design strategy for ensuring fast and stable Na storage may work with other electrode materials as well.

1 Introduction

With the recent increases in the consumption of fossil fuels and the resulting increase in environmental pollution, the development of advanced energy storage and conversion devices has become a necessity [1]. As the most promising alternatives to lithium-ion batteries (LIBs), rechargeable sodium-ion batteries (SIBs) are receiving increasing attention for use in large-scale energy storage applications, given the natural abundance of Na [2, 3]. However, one of the challenges for the commercialization of Na-ion batteries

Address correspondence to yong.lei@tu-ilmenau.de

is the development of suitable anodic materials for hosting the Na ions, which have a larger radius than that of Li ions [4, 5]. Commercial graphite, which is used widely as an anodic material in LIBs, does not react effectively with sodium, owing to its poor intercalation because of the larger radius of Na^+ ions [6]. Of the various anodic materials being explored, metallic Sb is particularly attractive because of its high theoretical capacity (660 $mAh \cdot g^{-1}$) and relatively safe operating potential of ~0.4 V (vs. Na^+/Na) [7, 8]. However, despite these advantages, Sb anodes find limited use because of the large changes that are induced in their volume (~390%) during cycling [9, 10]; this is because Sb materials undergo pulverization readily and are thus electrically isolated from the current collector. This leads to rapid capacity degradation and poor rate capability [5, 11].

An effective method of addressing this issue of volume change is to design integrated electrodes in which nanosized active materials are grafted onto a secondary matrix [12–16]. Such electrodes can not only accommodate large volume changes but also show improved ion accessibility and fast electron transport; these three characteristics are indispensable for ensuring high electrochemical performance. Because the electrochemical properties of a material are intimately related to its design and properties at the nanoscale, increasing attention is being paid to designing metallic Sb materials with novel morphologies, especially in terms of the particle size and interparticle distance [17–19]. Previous studies have shown that decreasing the dimensions of Sb materials to the nanometer range enhances their tolerance to changes in stress during alloying/dealloying and shortens the electronic and ionic transport pathways, resulting in high capacity, long cycling life, and good rate capability [20–22]. For instance, monodispersed antimony nanocrystals were used as SIB anodes; these anodes exhibited capacities of approximately 550 and 520 $mAh \cdot g^{-1}$ at current densities of 5.28 and 13.2 $A \cdot g^{-1}$, respectively [18]. Similarly, a nanoporous antimony anode showed a capacity as high as 573.8 $mAh \cdot g^{-1}$ after 200 cycles at a rate of 100 $mA \cdot g^{-1}$ [23]. Recently, nanoplates have also attracted attention owing to their unique structural and mechanical strengths and high surface-to-volume ratio. Nanoplates-based electrode materials exhibit short ion diffusion lengths. Further, the surface contact area between the electrolyte and the conductive material is large, leading to improved capacitive charge storage and hence excellent rate performance and high power density.

Three-dimensional (3D) nanoarrayed current collectors have been used successfully as the secondary matrix for the grafting of active materials to form electrodes. The 3D open and conductive network creates open channels and increases the contact area between the current collector and the active material, resulting in fast ion/electron transport as well as a large electrode/electrolyte interfacial area. The resulting unique 3D core/shell structures effectively inhibit the aggregation of the active material. As a result, the composite material can better accommodate the large volume changes induced during cycling [24–28]. Conventional electrodes usually have a flat structure and contain inactive additives such as polymeric binders, which often suffer from insufficient ion permeation. In addition, insulating binders block electron transport [29, 30]. In contrast, the use of 3D additive-free nanoarrayed electrodes that do not require complex fabrication processes and show excellent electrical conductivity and self-integrity can efficiently resolve these issues [31, 32], leading to enhanced cycling life and high rate capability [24–33].

Herein, we designed a novel 3D nanostructured Sb anode material, that is, hierarchical anodes composed of Sb nanoplates formed on Ni nanorod arrays (3D Sb-Ni nanoarrays), for use in high-performance SIBs. This heterostructured electrode material combines the advantages of 2D nanoplates and an open and conductive array structure, while also exhibiting strong structural integrity. The structure of the material significantly promotes electron and ion transport and can accommodate large volume changes. Further, when used as binder-free SIB anodes, the 3D Sb-Ni nanoarrays showed high capacity, long cycling life, and excellent rate capability not only in Na-ion half cells but also in full cells. These results should improve our understanding of SIB anodes and aid the development of material engineering strategies for improving the performance of SIBs.

2 Results and discussion

2.1 Structural characterization

The strategy used for fabricating the 3D Sb-Ni nanoarrays is depicted schematically in Fig. 1. First, a through-pore anodized aluminum oxide (AAO) template with a conductive substrate (Fig. 1(a)) was prepared as per a previously reported method [34]. The scanning electron microscopy (SEM) image in Fig. 1(d) shows clearly a uniform AAO template with a pore size of approximately 210 nm. Next, 3D Ni nanorod arrays were fabricated by electrodeposition through the AAO template, which was subsequently dissolved (Fig. 1(b)). It can be seen from Fig. 1(e) that the Ni nanorods are smooth and vertically aligned with respect to the substrate, with the diameter of the nanorods being 210 nm and the interrod spacing being 190 nm. These unique Ni nanorod arrays could be used as efficient current collectors and skeletons for the direct and spontaneous deposition of the active material, resulting in a high specific surface area and a large number of active sites. The fabrication process was completed by growing Sb nanoplates on the Ni nanorod arrays by electrodeposition under vacuum. This yielded 3D Sb-Ni nanoarrays that exhibited robust adhesion and could be used as binder-free SIB anodes, as shown in Fig. 1(c). Further, this electrode configuration allowed for rapid ion/electron transport, resulted in a large electrode/electrolyte interfacial area, and could accommodate the volume changes induced during cycling, thus ensuring the stability of the electrode structure. Figure 1(f) highlights the high quality and uniform nature of the 3D Sb-Ni nanoarrays even when fabricated on a large scale; the rough surfaces of the arrays confirm the successful deposition of Sb. Moreover, the interspacing between the formed arrays is uniform, suggesting improved electrolyte penetration and the ability to accommodate large volume changes. The magnified SEM image in Fig. 1(g) confirms the formation of Sb nanoplates on the Ni nanorod arrays; the Sb shells are composed of randomly oriented nanoplates, which form a hierarchical architecture. A single Sb-Ni nanorod is displayed in Figs. 1(h) and 1(i); as was also seen in the above-described SEM images, the Sb nanoplates, which have a thickness of 20 nm, intercross each other, forming a highly porous nanoarchitecture with abundant open areas and a large number of electroactive surface sites.

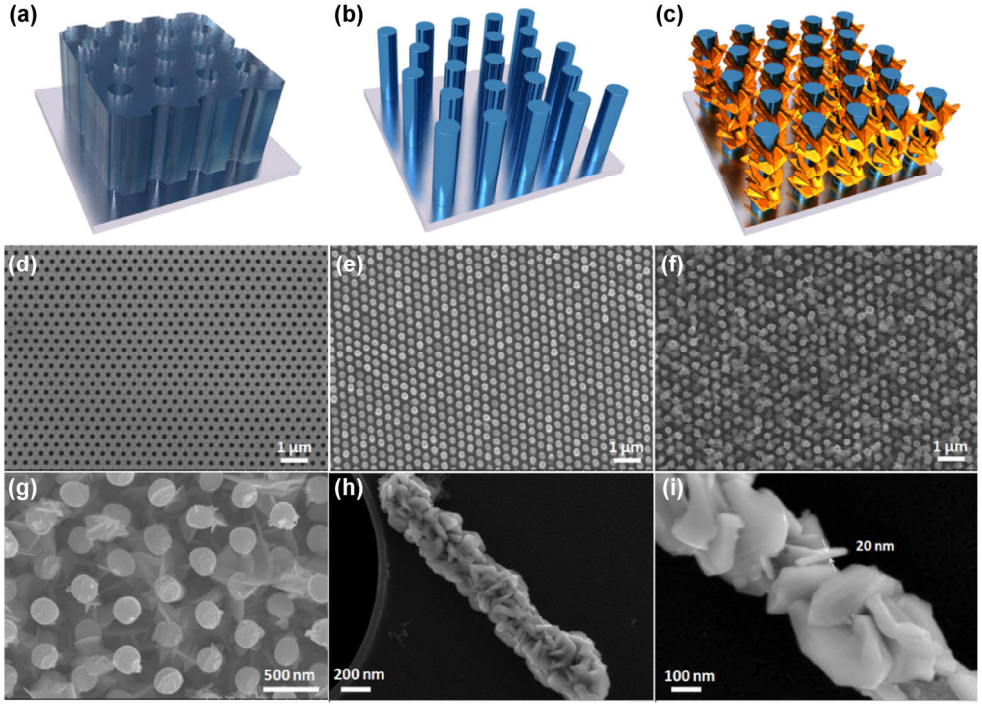

Figure 1 (a) Schematic illustration of AAO template, (b) Ni nanorod arrays, and (c) 3D Sb-Ni nanoarrays. SEM images of (d) AAO template, (e) Ni nanorod arrays, and (f)–(i) 3D Sb-Ni nanoarrays.

The crystalline phases of the fabricated composite material were investigated using X-ray diffraction (XRD) analysis, as shown in Fig. 2(a). All the peaks except for those related to the substrate (Au) and current collector (Ni) are attributable to rhombohedral Sb (JCPDS No. 35-0732), confirming the successful fabrication of the Sb/Ni heterostructure. The fabricated hierarchical structure was characterized further using high-resolution transmission electron microscopy (HRTEM). Figures 2(b)–2(d) shows a dark-field SEM image, line scan profile, and energy-dispersive X-ray spectroscopy (EDX) mapping results of a single Sb-Ni nanorod, confirming that the Sb nanoplates are uniformly distributed on the surfaces of the Ni nanorods. An HRTEM image of a typical Sb-Ni nanorod is shown in Fig. 2(e); it can be seen that irregular Sb nanoplates are firmly anchored on the Ni backbone. Figure 2(f) shows that the Sb crystallites have a distinct lattice spacing, with the lattice fringes with spacings of 0.310 and 0.354 nm corresponding to the (012) and (101) planes, respectively, of rhombohedral Sb. The fast Fourier transform (FFT) pattern in the inset of Fig. 2(f) inset confirms the single-crystalline nature of Sb.

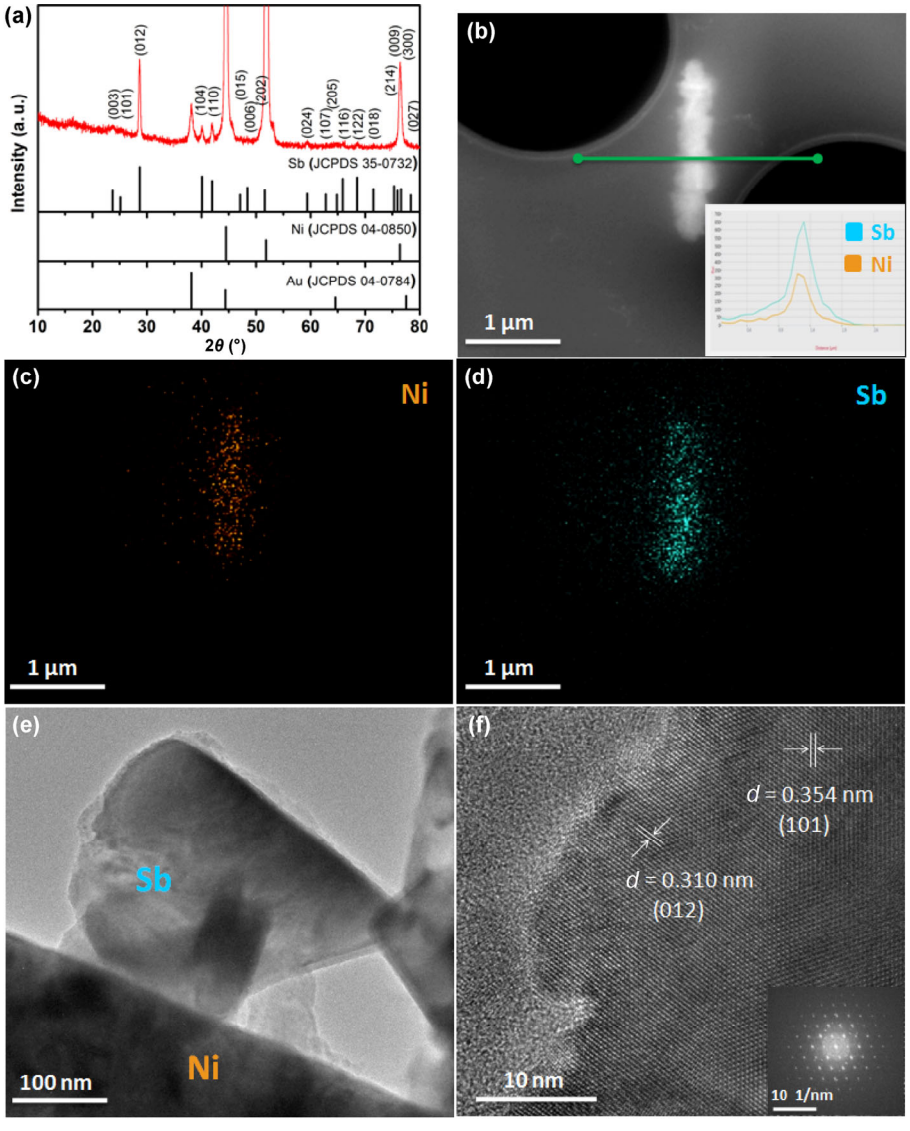

Figure 2 (a) XRD pattern of 3D Sb-Ni nanoarrays. (b) Dark-field SEM image of individual Sb-Ni nanorod and corresponding line scan profile (inset of (b)). EDX maps for elemental (c) Ni and (d) Sb. HRTEM images of Sb-Ni nanorod (e) and Sb nanoplate (f) and FFT pattern (inset of (f)).

2.2 Na-ion half-cell performance

Given the unique structure of the 3D Sb-Ni nanoarrays, they were employed as binder-free anodes in a Na-ion half-cell. Figure 3(a) shows the representative cyclic voltammograms (CVs) of the cell for the first three cycles at a scan rate of 0.1 $mV \cdot s^{-1}$. Two strong broad peaks, located at 0.42 and 0.37 V, can be observed during the first sodiation scan; these are ascribable to the formation of a solid electrolyte interface (SEI) layer and an amorphous Na_xSb alloy phase, which is subsequently transformed into cubic and hexagonal Na_3Sb through further sodiation [35–37]. During the second sodiation scan, three distinct peaks are observed, at 0.67, 0.43 and 0.37 V; these correspond to the multistep sodiation reactions between the Sb and Na ions, which result in the formation of a hexagonal Na_3Sb alloy [36–38]. The difference in the first and second sodiation scans can primarily be ascribed to the formation of the SEI layer and the rearrangement of the anode structure [38–40]. During the desodiation scans, a broad peak ranging from 0.70 to 0.96 V is observed; it is attributable to the phase transformation from Na_3Sb to Sb [35–37]. The galvanostatic charge/discharge curves of the 3D Sb-Ni nanoarrays as anodes at a current density of 0.5 $A \cdot g^{-1}$ are shown in Fig. 3(b); it can be seen that the curves exhibit characteristics typical of Sb anodes. The voltage profiles with different plateaus are indicative of the redox reactions associated with Na alloying and dealloying during discharging and charging, in keeping with the CVs shown in Fig. 3(a). Furthermore, the voltage profiles corresponding to both sodiation and desodiation show excellent reproducibility from 1 to 100 cycles, highlighting the structural stability of the 3D Sb-Ni nanoarrays as well as the high reversibility of the electrochemical reactions occurring during cycling [38].

The cyclic performance of the 3D Sb-Ni nanoarrays as anodes was investigated at current densities of 0.5 and 1.0 $A \cdot g^{-1}$. As shown in Fig. 3(c), the anodes show large reversible capacities and high capacity retention rates, which can be attributed to their unique hierarchical structure. For example, at a current density of 0.5 $A \cdot g^{-1}$, the anodes exhibit a reversible capacity of 623 $mAh \cdot g^{-1}$ after the 100th cycle; this value is close to the theoretical capacity of Sb (660 $mAh \cdot g^{-1}$). The capacity retention rates after 200 cycles are as high as 80% and 72% at 0.5 and 1.0 $A \cdot g^{-1}$, respectively. These values are much higher than most of those reported for other Sb-based anodes [8, 10, 34, 35, 41]. The capacity fading of the 3D Sb-Ni nanoarrays can be ascribed to the increase in the thickness of the SEI layer and the inevitable volume changes induced during cycling. The coulombic efficiency (CE) is close to 98% at both 0.5 and 1.0 $A \cdot g^{-1}$ for all the cycles except the initial ones, suggesting that ion and electron transport occur readily in the 3D Sb-Ni nanoarrays anodes [40, 42, 43].

To investigate the effects of the 3D heterostructured configuration of the composite material on its rate capability, the 3D Sb-Ni nanoarrays anodes were galvanostatically tested at various current densities (0.2–20 $A \cdot g^{-1}$). As can be seen from Fig. 3(d), the 3D Sb-Ni nanoarrays show excellent rate characteristics. They could be reversibly cycled at rates as high as 10 and 20 $A \cdot g^{-1}$ while show a high CE (approximately 98%). During the second rate test, the 3D Sb-Ni nanoarrays as anodes were cycled five times at each current rate. The capacity remained stable at each rate, regardless of the rate cycling history. More notably, during the second set, they exhibited high capacities, of 607 and 580 $mAh \cdot g^{-1}$ at 10 and 20 $A \cdot g^{-1}$, respectively; these results are indicative of rapid Na ion and electron transfer through the 3D Sb-Ni nanoarrays anodes. During further cycling at a low rate of 0.5 $A \cdot g^{-1}$ during the third rate test, the capacity retention was approximately 94% of that at the same rate during the first set, indicating that the structure of the 3D Sb-Ni nanoarrays remained relatively stable even when the rate was varied, with the nanoarrays simultaneously exhibiting high energy densities. This rate capability and the observed specific capacities are among the best reported for Sb-based anodes (Fig. 3(e)). Figure 3(f) shows the corresponding voltage profiles of the anodes at various current densities, as measured during the first set. Even as the current density is increased from 0.2 to 20 $A \cdot g^{-1}$, the charge and discharge voltage profiles exhibit similar shapes, with the increase in the voltage offset being minimal. Furthermore, in the second set, when the anodes are cycled again at 0.5, 1.0, 0.5, and 10 $A \cdot g^{-1}$, the voltage profiles recover and are very similar to those of the first set for the same current densities (Fig. S1 in the

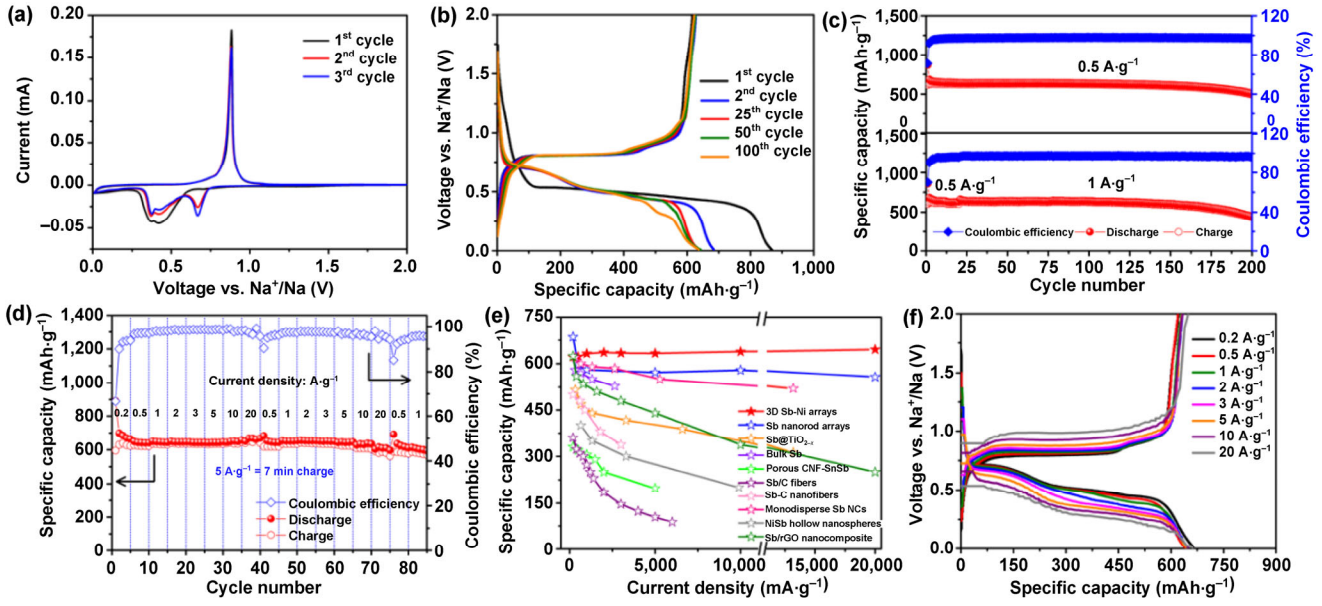

Figure 3 Electrochemical performance of 3D Sb-Ni nanoarrays anodes. (a) CVs at scan rate of 0.1 mV·s^{-1} between 0.01 to 2.0 V (vs. Na^+/Na). (b) Galvanostatic charge/discharge voltage profiles for different numbers of cycles at current density of 0.5 A·g^{-1}. (c) Cycling performance at current densities of 0.5 and 1.0 A·g^{-1}. (d) Rate performance at various current densities (0.1–20 A·g^{-1}). (e) Ragone plots of 3D Sb-Ni nanoarrays anodes and other previously reported Sb-based SIBs anodes (Sb nanorod arrays: Ref. [34], Sb@TiO_{2-x}: Ref. [20], bulk Sb: Ref. [35], porous CNF-SnSb: Ref. [38], Sb-C nanofibers: Ref. [10], monodisperse Sb NCs: Ref. [18], NiSb hollow nanospheres: Ref. [21], Sb/rGO nanocomposites: Ref. [44], and Sb/C fibers: Ref. [40]). (f) Charge/discharge voltage profiles at various current densities (0.1–20 A·g^{-1}).

Electronic Supplementary Material (ESM)). All these features indicate that electron transport occurs readily in the 3D Sb-Ni nanoarrays anodes and that the mechanical energy loss in the anodes is minimal.

2.3 Kinetics and quantitative analysis of Na^+ storage mechanism

To explain the high rate performance, the electrochemical kinetics of the 3D Sb-Ni nanoarrays were analyzed through cyclic voltammetry. Figure 4(a) shows that the CVs obtained at various scan rates (0.1–10 mV·s^{-1}) are very similar. It is known that the CVs of an electrode material can be used to distinguish between the contributions of the diffusion process and the capacitance to the underlying electrochemical reaction based on the slope (i.e., b value), which is calculated from the plot of the log (peak current, i_p) vs. the log (scan rate, v) [45]. Usually, b values of 1 and 0.5 indicate that the electrochemical reaction is surface limited and diffusion limited, respectively, with the former corresponding to capacitive behavior and Na^+ ion insertion/extraction. Generally, the b value is 0.5–1, implying that both phenomena contribute to the reaction. As can be seen from Fig. 4(b), the b values corresponding to the three cathodic peaks seen in the case of the 3D Sb-Ni nanoarrays anodes are 0.82, 0.78 and 0.84, indicating that the Na-storage reactions in the 3D Sb-Ni nanoarrays are capacitive in nature. Furthermore, the contribution of the total capacity (Q) storage can be analyzed using Trasatti's method, which describes the relationship between the capacity and the sweep rate [46]. The Q value involves both the capacity related to the surface process (Q_s) and that related to the diffusion-controlled process (Q_d), as shown in Eq. (1)

$$Q(v) = Q_s + Q_d = Q_s + k(v^{-1/2}) \quad (1)$$

Here, k is a constant and v is the potential scan rate. Further, Q_d is the diffusion-controlled capacity, which is limited by $v^{-1/2}$. The surface capacity (Q_s) remains constant with the scan rate, which can be determined from the plot of the capacity (Q) vs. $v^{-1/2}$. The extrapolation of the linear fit of the data to the y-axis ($v^{-1/2} = 0$) gives the capacitive contribution (Q_s), which

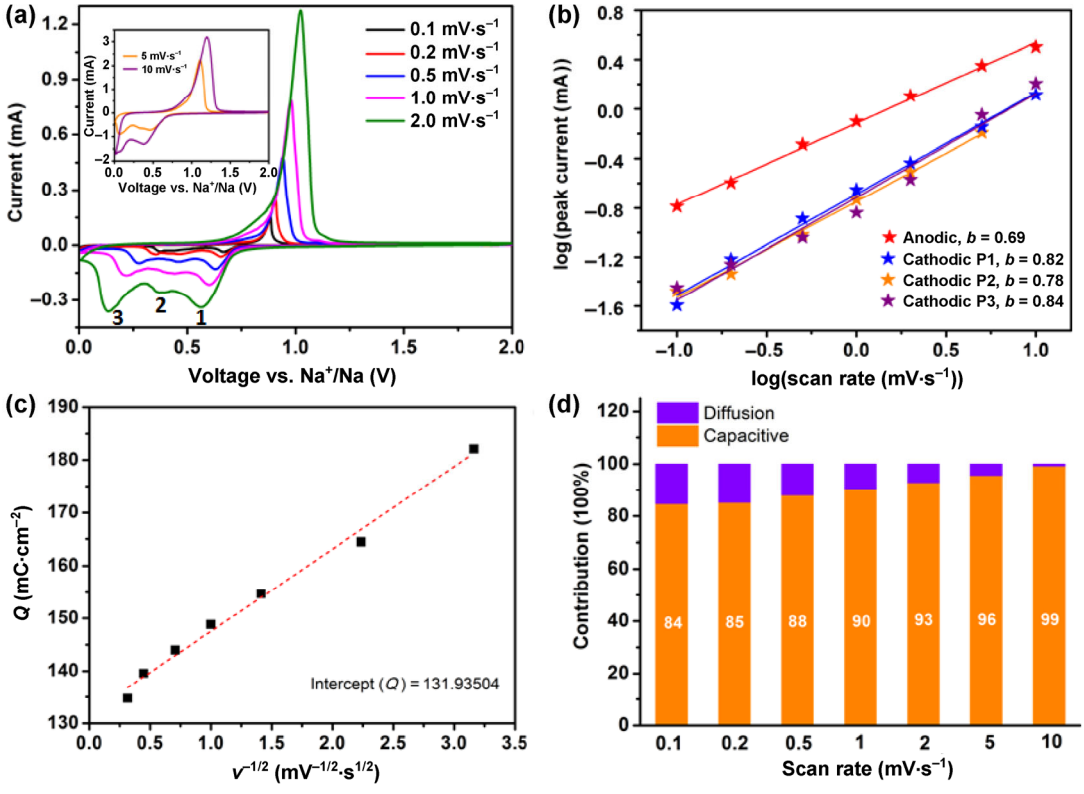

Figure 4 Kinetics and quantitative analysis of Na^+ storage mechanism. (a) CVs of 3D Sb-Ni nanoarrays at different scan rates (0.1–10 $mV·s^{-1}$). (b) Plots of log i_p vs. log v for cathodic/anodic peaks. (c) Trasatti analysis based on dependence of charge storage on reciprocal square root of scan rate. In the plot of capacity (Q) vs. $v^{-1/2}$, the y-intercept corresponds to the infinite-sweep-rate capacity, $Q_{v=\infty}$. (d) Normalized contribution ratio of capacitive (orange yellow) and diffusion-controlled (blue) capacities at different scan rates as calculated through Trasatti analysis using Eq. (1).

was calculated to be 131.9 $mC·cm^{-2}$ (Fig. 4(c)). Moreover, the relative contributions of the capacitive and diffusion-controlled processes could be elucidated, as shown in Fig. 4(d). As the scan rate is increased, the capacitive contribution also increases. The contribution is 84% at a scan rate of 0.1 $mV·s^{-1}$ but increases to 99% at 10 $mV·s^{-1}$. It has been reported that the capacitive contribution plays a greater role in the case of structures with a high surface area and/or high porosity [14, 47, 48]. Generally, the greater the capacitance, the better is the rate capability [20, 45]. This fact explains the excellent rate performance of the 3D Sb-Ni nanoarrays. To the best of our knowledge, such a stable and robust rate capability has not been reported previously for Sb-based anodes, which underlines the effectiveness of the electrode design used.

2.4 Na-ion full cell performance

To further explore the practical suitability of the 3D Sb-Ni nanoarrays for Na storage, a full cell was fabricated using the 3D Sb-Ni nanoarrays as the negative electrodes and P2-$Na_{2/3}Ni_{1/3}Mn_{2/3}O_2$ as the material for the positive electrodes. The structure and electrochemical performance of P2-$Na_{2/3}Ni_{1/3}Mn_{2/3}O_2$ have been reported in our previous work [34]. This full cell was tested in a potential window of 1.4–4.0 V. Figure 5(a) displays the CVs of the full cell at a scan rate of 0.5 $mV·s^{-1}$. The cathodic and anodic peaks at 3.4 and 3.7 V correspond to the insertion/extraction of Na^+ ions into/from P2-$Na_{2/3}Ni_{1/3}Mn_{2/3}O_2$. The pairs of peaks at 2.8/3.2 V and 2.77/3.0 V are attributable to the sodiation of Sb and the desodiation of Na_3Sb. That multiple redox reactions occurred is also reflected in the charge/discharge voltage profile of the full cell (Fig. 5(a) inset), which is in good agreement with the CVs. The excellent reproducibility of the CVs further confirms the high stability of the electrode material. Figure 5(b) shows the cycling performance of the full

cell; it can be seen that the cell delivers a highly stable capacity over 200 cycles at a current density of 0.5 $A \cdot g^{-1}$. After 200 charge/discharge cycles, it retains a reversible capacity of 579.8 $mAh \cdot g^{-1}$ (relative to the mass of the Sb anodes), which is 87.8% of the theoretical capacity of Sb (660 $mAh \cdot g^{-1}$). In addition, with the exception of the initial activation cycles, the cell shows a CE as high as 98%. The energy density is estimated to be approximately 100 $Wh \cdot kg^{-1}$ (based on the total mass of the positive and negative active materials), which is an extremely high value [1]. Furthermore, the full cell exhibits a high rate capability, as seen in Fig. 5(c). It can be cycled at very high rates (10 and 20 $A \cdot g^{-1}$) and shows stable reversibility, exhibiting capacities of 526.3 and 434.2 $mAh \cdot g^{-1}$, respectively, in the second set. These values correspond to charge times of 3 min 23 s and 1 min 40 s (Fig. 5(d)), respectively, which are sufficient for high-rate applications [49]. For various current densities (0.2–20 $A \cdot g^{-1}$), after 75 cycles, these capacities are recovered when the cell again shows a low current density, delivering a capacity of 539.5 $mAh \cdot g^{-1}$ at 0.5 $A \cdot g^{-1}$. Although the current density increases markedly (by a factor of 100), the discharge voltage drops only by approximately 0.16 V, indicating that the full cell undergoes a low degree of polarization and that the reaction kinetics in the cell show desirable characteristics (Fig. 5(d)). Further, the electrochemical performance of the P2-$Na_{2/3}Ni_{1/3}Mn_{2/3}O_2$//3D Sb-Ni nanoarrays Na-ion full battery is superior to that of recently reported $Na_3V_2(PO_4)_3$-C//Sb@TiO_2 [20], $Na_{2/3}Ni_{1/3}Mn_{2/3}O_2$//rGO/$Sb_2S_3$ [49], and $Na_{0.4}Mn_{0.54}Co_{0.46}O_2$// NiSb full batteries [21].

2.5 Factors determining electrochemical performance

The excellent electrochemical performance of the 3D Sb-Ni nanoarrays as anodes can be attributed to their unique nanostructure. Specifically, their high capacity and excellent rate capability are mainly attributable to the following structural features. First, the distance for Na^+ ion diffusion in the Sb nanoplates is small and the electrode/electrolyte contact area is large, resulting in a high flux of Na^+ ions across the interface. Next, every Ni nanorod provides a direct and short pathway for electrons to the Sb nanoplates. Further, in these open and vertically aligned 3D nanostructured arrays, the electrolyte ions can move readily, resulting in the maximum utilization of the electroactive material at high rates. A possible interfacial Na storage effect in the Sb/Ni heterogeneous structure may also contribute to the improved electrochemical performance; this phenomenon has been observed in previous studies as well [50–54].

The ability to accommodate the large change in the volume of Sb is another extremely important criterion for ensuring good rate capability and cycling life. In this work, Sb nanoplates were grown on the Ni nanorod arrays; several features of the resulting nanostructures helped in accommodating these volume changes. To begin with, the Ni nanorods, which served as scaffolds, provided large surfaces for the growth of the Sb nanoplates. This resulted in the formation of well-dispersed and immobilized Sb nanoplates. Hence, the agglomeration of the active material was prevented. Meanwhile, the direct growth of the Sb nanoplates on the Ni nanorod backbones resulted in the firm bonding of the nanoplates to the current collectors, and the Ni skeletons could effectively suppress the adverse mechanical effects related to the large volume increase [55]. The improved capacity and cycling life of these assemblies of Sb nanoplates on Ni nanorod arrays are thus be related to their 3D design. For comparison, Figs. S2(a) and S2(b) in the ESM shows a planar Sb electrode fabricated on a piece of Ni foil by electrodeposition under the same conditions. The electrode, which is composed of highly aggregated Sb nanoplates, exhibits dramatic capacity fading upon cycling as well as significantly higher resistances than those of the 3D Sb-Ni nanoarrays (Figs. S2(c) and S2(d) in the ESM), owing to a large volume change and pulverization (Figs. S2(e) and S2(f) in the ESM). Second, the presence of sufficiently large interspacing between the arrays effectively mitigates the strain induced during the Na intercalation/deintercalation processes. As shown in Fig. S3(a) in the ESM, the interspacing between the nanorods was increasingly filled with Sb as the deposition time was increased; this would have reduced the accessibility of the electrolyte ions to the space between the rods (Fig. S4 in the ESM), thus preventing the volume buffering of Sb during discharging/charging. This is what resulted in poor capacity retention and rapid

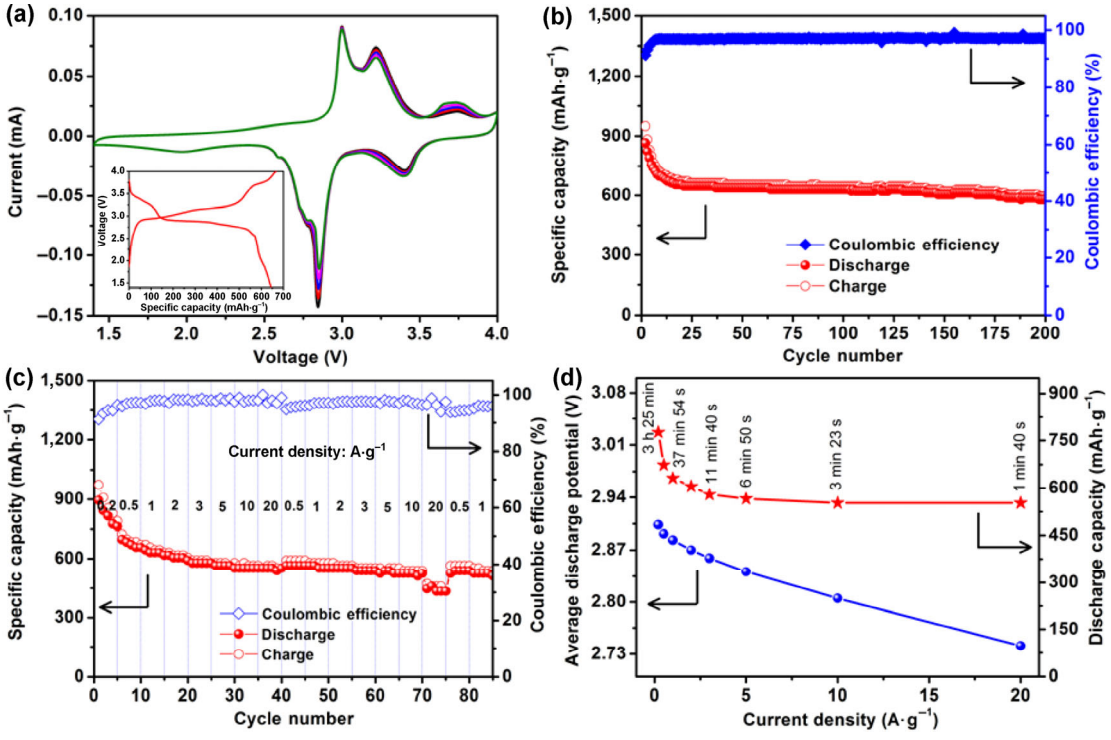

Figure 5 Electrochemical performance of full cell consisting of P2-$Na_{2/3}Ni_{1/3}Mn_{2/3}O_2$ cathodes and 3D Sb-Ni nanoarrays as anodes. (a) Cyclic voltammetry curves at scan rate of 0.5 $mV·s^{-1}$ and galvanostatic charge/discharge voltage profiles (inset) at current density of 0.5 $A·g^{-1}$. (b) Cycling performance at current density of 0.5 $A·g^{-1}$ (relative to anode weight) (starting from 2nd cycle). (c) Rate capability (with respect to anode weight) at various current densities (0.1–20 $A·g^{-1}$). (d) Respective discharge capacity and average discharge working potential at various current densities.

increases in the resistance (Figs. S3(b)–S3(d) in the ESM). Thus, a sufficiently large interspacing is critical in the case of nanostructured electrodes consisting of Sb nanoplates formed on Ni nanorods. Third, the void space between these plate-like subunits could accommodate the volume changes.

Last but most important, although the above strategies can assimilate the large volume changes to a certain extent, some change in the volume is inevitable, owing to the inherent nature of Sb. In particular, during further cycling, the mechanical breakdown of Sb is hard to prevent. The advantage of the 3D Sb-Ni nanoarrays is manifested when such a breakdown occurs. A distinct difference is observed in the case of bare 3D Sb nanorod arrays, wherein, owing to the loss of electrical contact with the conductive substrate, the sections of the nanorods beyond the cracking point become inaccessible (Fig. S5(a) in the ESM); this significantly reduces the overall capacity [34]. In contrast, in the case of the 3D Sb-Ni nanoarrays, this type of breakdown has a relatively limited effect on the overall capacity, as the Sb nanoplates that do not fall off are still connected to the Ni nanorods, as shown in Fig. S5(b) in the ESM. The overall capacity fades at a comparatively slower rate than is the case for the nanostructures consisting only of nanorods (Fig. S6 in the ESM). The morphology of the 3D Sb-Ni nanoarrays after cycling confirms this. Figures 6(a) and 6(b) shows SEM images of the cycled arrays, which are similar to those of the arrays before cycling, implying that this electrode structure can effectively accommodate the large volume changes that occur during sodiation/desodiation. After 200 discharge/charge cycles, owing to the repeated changes in the volume, the Sb nanoplates break into smaller nanoplates and their plate-like structure is crushed to a certain degree, resulting in the formation of a loose-packed structure (Fig. 6(c)). Despite this fact, most of the Sb nanoplates remain tightly attached to the Ni nanorods, showing only a small decay in capacity;

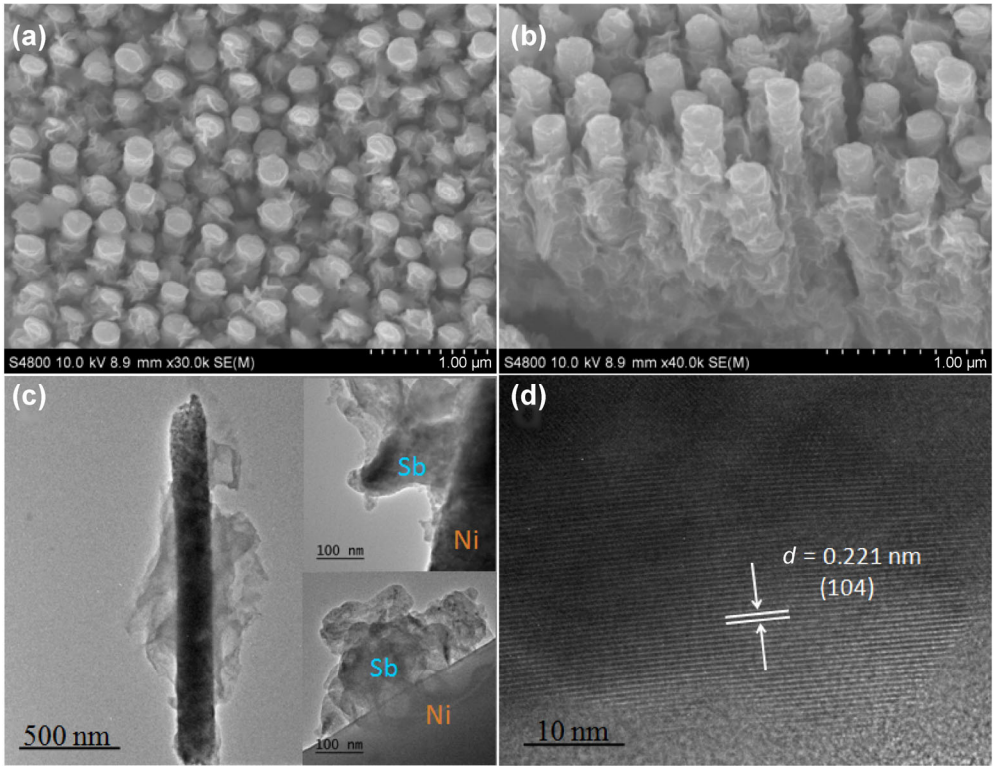

Figure 6 (a) and (b) SEM images and (c) and (d) HRTEM images of 3D Sb-Ni nanoarrays anodes after 200 cycles.

this is again indicative of the structural stability of the 3D Sb-Ni nanoarrays. Figure 6(d) shows the crystallinity of the 3D Sb-Ni nanoarrays after cycling. Distinct lattice spacing can be observed, with the lattice fringe with a spacing of 0.221 nm corresponding to the (104) plane of rhombohedral Sb.

3 Conclusions

In summary, we designed and synthesized hierarchical electrodes consisting of Sb nanoplates on Ni nanorod arrays. This novel functional heterostructure exhibits the synergistic effects of the 2D nanoplates and the open and conductive array structure as well as strong structural integrity. The results of a kinetics analysis confirmed that the Na storage process is surface controlled, clearly indicating that the Na reaction kinetics and the durability of the 3D Sb-Ni nanoarrays are attributable to their unique structure. When used as binder-free SIBs anodes, the 3D Sb-Ni nanoarrays exhibited remarkably improved electrochemical performance in both Na-ion half and full cells. It is expected that this design strategy will also be suitable for modulating other types of electrodes for advanced energy storage systems.

4 Experimental

4.1 Material synthesis

The through-pore AAO template formed on a conductive substrate was fabricated by an anodization process and a subsequent ion coating process. Details of these processes can be found in our previous work [34]. Ni nanorod arrays were electrodeposited within the AAO template at a constant current density of 2.0 $mA \cdot cm^{-2}$ in an electrolytic bath containing $NiCl_2$, $NiSO_4$, and H_3BO_3. The electrodeposition was performed in a two-electrode cell while using the AAO template as the working electrode and a piece of Ni foil as the counter electrode. The Ni nanorod arrays were released by dissolving the AAO template in a NaOH solution (3.0 M) for 30 min; this was followed by rinsing with deionized water. The Ni nanorod arrays were then immersed in an electrolytic bath containing $SbCl_3$ and $Na_3C_6H_5O_7 \cdot 2H_2O$ and then

placed in a vacuum oven for a while. The 3D Sb-Ni nanoarrays were prepared by electrodepositing Sb on the Ni nanorod arrays at a constant current density of 1.0 $mA \cdot cm^{-2}$. This electrodeposition process was also performed in a two-electrode cell while using the Ni nanorod arrays as the working electrode and a piece of Pt foil as the counter electrode.

4.2 Sample characterization

SEM imaging was performed on a Hitachi S4800 instrument at a voltage of 10 kV. The HRTEM images were taken on a FEI Titan 80-300 system operated at 300 kV. The XRD measurements were performed on a Bruker-AXS Discover D8 system with a Cu Kα (1.54056 Å) radiation source. For post-cycling SEM imaging, the 3D Ni-Sb arrays subjected to the electrochemical cycling tests were disassembled with care, washed with a propylene carbonate (PC) solution in a glove box, and dried at 60 ℃ in a vacuum oven.

4.3 Electrochemical measurements

The electrochemical measurements involving the half cells were performed using CR2032 coin-type cells. Na metal was used as both the counter and the reference electrode, while the 3D Sb-Ni nanoarrays were employed as the anodes; no additives such as conductive carbon or binder were used. The coin batteries were assembled in a nitrogen-filled glove box with a glass fiber separator (Whatman, GFB/55); the electrolyte used was a solution of 1.0 M $NaClO_4$ in ethylene carbonate (EC)/PC (1:1 by volume) and containing 5% fluoroethylene carbonate (FEC). The galvanostatic charge/discharge tests were performed at various current densities on a LAND-CT2001A test system (Wuhan, China). The CVs were measured on a BioLogic VSP potentiostat. Electrochemical impedance spectroscopy (EIS) measurements were performed on a BioLogic VSP potentiostat at frequencies of 1 MHz to 10 mHz at the charge state (2.0 V). All the measurements were conducted at room temperature.

The electrochemical measurements involving full cells were performed using CR2032 coin-type cells with 3D Ni-Sb nanoarrays as the negative electrodes and P2-$Na_{2/3}Ni_{1/3}Mn_{2/3}O_2$ as the positive electrode material. P2-$Na_{2/3}Ni_{1/3}Mn_{2/3}O_2$ was prepared by mixing 80% P2-$Na_{2/3}Ni_{1/3}Mn_{2/3}O_2$, 10% acetylene black, and 10% poly(vinylidene fluoride) by weight with an appropriate amount of 1-methyl-2-pyrrolidinone. The above mixture was pressed onto an aluminum foil, which served as the current collector. The cathode was formed by drying at 120 ℃ in vacuum for 12 h. The full cell was assembled using an electrolyte solution consisting of 1.0 M $NaClO_4$ in EC/PC (1:1 by volume) and 5% FEC and was galvanostatically cycled for voltages of 1.4–4.0 V. To ensure a suitable positive-to-negative capacity ratio for cell balance, the P2-$Na_{2/3}Ni_{1/3}Mn_{2/3}O_2$/Sb nanorod arrays mass loading ratio was kept at approximately 20.

Acknowledgements

This work is financially supported by the European Research Council (ThreeDsurface, No. 240144), European Research Council (HiNaPc, No. 737616), BMBF (ZIK-3DNanoDevice, No. 03Z1MN11), and German Research Foundation (DFG: LE 2249_4-1).

Electronic Supplementary Material: Supplementary material (voltage profiles at various current densities in different sets, SEM images and electrochemical performance of planar Sb electrode on Ni foil and 3D Sb-Ni nanoarrays with insufficient interspace, schematic illustration of transport mechanism of Na ions in various Sb structures, comparison of cycling performance between bare Sb nanorod arrays and 3D Sb-Ni nanoarrays) is available in the online version of this article at https://doi.org/10.1007/s12274-017-1536-0.

References

[1] Hasa, I.; Passerini, S.; Hassoun, J. A rechargeable sodium-ion battery using a nanostructured Sb–C anode and P2-type layered $Na_{0.6}Ni_{0.22}Fe_{0.11}Mn_{0.66}O_2$ cathode. *RSC Adv.* **2015**, *5*, 48928–48934.

[2] Palomares, V.; Serras, P.; Villaluenga, I.; Hueso, K. B.; Carretero-González, J.; Rojo, T. Na-ion batteries, recent advances and present challenges to become low cost energy storage systems. *Energy Environ. Sci.* **2012**, *5*, 5884–5901.

[3] Kim, S. W.; Seo, D. H.; Ma, X. H.; Ceder, G.; Kang, K. Electrode materials for rechargeable sodium-ion batteries: Potential alternatives to current lithium-ion batteries. *Adv. Energy Mater.* **2012**, *2*, 710–721.

[4] Hong, S. Y.; Kim, Y.; Park, Y.; Choi, A.; Choi, N.-S.; Lee, K. T. Charge carriers in rechargeable batteries: Na ions vs. Li ions. *Energy Environ. Sci.* **2013**, *6*, 2067–2081.

[5] Slater, M. D.; Kim, D.; Lee, E.; Johnson, C. S. Sodium-ion batteries. *Adv. Funct. Mater.* **2013**, *23*, 947–958.

[6] Stevens, D. A.; Dahn, J. R. High capacity anode materials for rechargeable sodium-ion batteries. *J. Electrochem. Soc.* **2000**, *147*, 1271–1273.

[7] Jeong, G.; Kim, Y.-U.; Kim, H.; Kim, Y.-J.; Sohn, H.-J. Prospective materials and applications for Li secondary batteries. *Energy Environ. Sci.* **2011**, *4*, 1986–2002.

[8] Hu, L. Y.; Zhu, X. S.; Du, Y. C.; Li, Y. F.; Zhou, X. S.; Bao, J. C. A chemically coupled antimony/multilayer graphene hybrid as a high-performance anode for sodium-ion batteries. *Chem. Mater.* **2015**, *27*, 8138–8145.

[9] Xu, Y. H.; Liu, Q.; Zhu, Y. J.; Liu, Y. H.; Langrock, A.; Zachariah, M. R.; Wang, C. S. Uniform nano-Sn/C composite anodes for lithium ion batteries. *Nano Lett.* **2013**, *13*, 470–474.

[10] Xiao, L. F.; Cao, Y. L.; Xiao, J.; Wang, W.; Kovarik, L.; Nie, Z. M.; Liu, J. High capacity, reversible alloying reactions in SnSb/C nanocomposites for Na-ion battery applications. *Chem. Commun.* **2012**, *48*, 3321–3323.

[11] Chevrier, V. L.; Ceder, G. Challenges for Na-ion negative electrodes. *J. Electrochem. Soc.* **2011**, *158*, A1011–A1014.

[12] Wu, L.; Lu, H. Y.; Xiao, L. F.; Ai, X. P.; Yang, H. X.; Cao, Y. L. Electrochemical properties and morphological evolution of pitaya-like Sb@C microspheres as high-performance anode for sodium ion batteries. *J. Mater. Chem. A* **2015**, *3*, 5708–5713.

[13] Xie, X. Q.; Kretschmer, K.; Zhang, J. Q.; Sun, B.; Su, D. W.; Wang, G. X. Sn@CNT nanopillars grown perpendicularly on carbon paper: A novel free-standing anode for sodium ion batteries. *Nano Energy* **2015**, *13*, 208–217.

[14] Chao, D. L.; Zhu, C. R.; Yang, P. H.; Xia, X. H.; Liu, J. L.; Wang, J.; Fan, X. F.; Savilov, S. V.; Lin, J. Y.; Fan, H. J. et al. Array of nanosheets render ultrafast and high-capacity Na-ion storage by tunable pseudocapacitance. *Nat. Commun.* **2016**, *7*, 12122.

[15] Lee, G.-H.; Shim, H.-W.; Kim, D.-W. Superior long-life and high-rate Ge nanoarrays anchored on Cu/C nanowire frameworks for Li-ion battery electrodes. *Nano Energy* **2015**, *13*, 218–225.

[16] Song, X. S.; Li, X. F.; Bai, Z. M.; Yan, B.; Li, D. J.; Sun, X. L. Morphology-dependent performance of nanostructured Ni_3S_2/Ni anode electrodes for high performance sodium ion batteries. *Nano Energy* **2016**, *26*, 533–540.

[17] Ko, Y. N.; Kang, Y. C. Electrochemical properties of ultrafine Sb nanocrystals embedded in carbon microspheres for use as Na-ion battery anode materials. *Chem. Commun.* **2014**, *50*, 12322–12324.

[18] He, M.; Kravchyk, K.; Walter, M.; Kovalenko, M. V. Monodisperse antimony nanocrystals for high-rate Li-ion and Na-ion battery anodes: Nano versus bulk. *Nano Lett.* **2014**, *14*, 1255–1262.

[19] Hou, H. S.; Jing, M. J.; Yang, Y. C.; Zhu, Y. R.; Fang, L. B.; Song, W. X.; Pan, C. C.; Yang, X. M.; Ji, X. B. Sodium/lithium storage behavior of antimony hollow nanospheres for rechargeable batteries. *ACS Appl. Mater. Interfaces* **2014**, *6*, 16189–16196.

[20] Wang, N.; Bai, Z. C.; Qian, Y. T.; Yang, J. Double-walled Sb@TiO_{2-x} nanotubes as a superior high-rate and ultralong-lifespan anode material for Na-ion and Li-ion batteries. *Adv. Mater.* **2016**, *28*, 4126–4133.

[21] Liu, J.; Yang, Z. Z.; Wang, J. Q.; Gu, L.; Maier, J.; Yu, Y. Three-dimensionally interconnected nickel–antimony intermetallic hollow nanospheres as anode material for high-rate sodium-ion batteries. *Nano Energy* **2015**, *16*, 389–398.

[22] Zhang, N.; Liu, Y. C.; Lu, Y. Y.; Han, X. P.; Cheng, F. Y.; Chen, J. Spherical nano-Sb@C composite as a high-rate and ultra-stable anode material for sodium-ion batteries. *Nano Res.* **2015**, *8*, 3384–3393.

[23] Liu, S.; Feng, J. K.; Bian, X. F.; Liu, J.; Xu, H. The morphology-controlled synthesis of a nanoporous-antimony anode for high-performance sodium-ion batteries. *Energy Environ. Sci.* **2016**, *9*, 1229–1236.

[24] Wang, J. Z.; Du, N.; Zhang, H.; Yu, J. X.; Yang, D. R. Cu–Ge core–shell nanowire arrays as three-dimensional electrodes for high-rate capability lithium-ion batteries. *J. Mater. Chem.* **2012**, *22*, 1511–1515.

[25] Lee, C. W.; Kim, J.-C.; Park, S.; Song, H. J.; Kim, D.-W. Highly stable sodium storage in 3-D gradational Sb–NiSb–Ni heterostructures. *Nano Energy* **2015**, *15*, 479–489.

[26] Xu, Y.; Zhou, M.; Wen, L. Y.; Wang, C. L.; Zhao, H. P.; Mi, Y.; Liang, L. Y.; Fu, Q.; Wu, M. H.; Lei, Y. Highly ordered three-dimensional Ni-TiO_2 nanoarrays as sodium ion battery anodes. *Chem. Mater.* **2015**, *27*, 4274–4280.

[27] Ke, F.-S.; Huang, L.; Solomon, B. C.; Wei, G.-Z.; Xue, L.-J.; Zhang, B.; Li, J.-T.; Zhou, X.-D.; Sun, S.-G. Three-dimensional nanoarchitecture of Sn–Sb–Co alloy as an anode of lithium-ion batteries with excellent lithium storage performance. *J. Mater. Chem.* **2012**, *22*, 17511–17517.

[28] Wang, J. Z.; Du, N.; Zhang, H.; Yu, J. X.; Yang, D. R. Cu–Sn core–shell nanowire arrays as three-dimensional electrodes for lithium-ion batteries. *J. Phys. Chem. C* **2011**, *115*, 23620–23624.

[29] Ryou, M. H.; Kim, J.; Lee, I.; Kim, S.; Jeong, Y. K.; Hong, S.; Ryu, J. H.; Kim, T. S.; Park, J. K.; Lee, H. et al. Mussel-inspired adhesive binders for high-performance silicon nanoparticle anodes in lithium-ion batteries. *Adv. Mater.* **2013**, *25*, 1571–1576.

[30] Zhao, F. P.; Han, N.; Huang, W. J.; Li, J. J.; Ye, H. L.; Chen, F. J.; Li, Y. G. Nanostructured CuP_2/C composites as high-performance anode materials for sodium ion batteries.

J. Mater. Chem. A **2015**, *3*, 21754–21759.

[31] Ellis, B. L.; Knauth, P.; Djenizian, T. Three-dimensional self-supported metal oxides for advanced energy storage. *Adv. Mater.* **2014**, *26*, 3368–3397.

[32] Fan, M. P.; Chen, Y.; Xie, Y. H.; Yang, T. Z.; Shen, X. W.; Xu, N.; Yu, H. Y.; Yan, C. L. Half-cell and full-cell applications of highly stable and binder-free sodium ion batteries based on Cu_3P nanowire anodes. *Adv. Funct. Mater.* **2016**, *26*, 5019–5027.

[33] Liu, Y. H.; Xu, Y. H.; Zhu, Y. J.; Culver, J. N.; Lundgren, C. A.; Xu, K.; Wang, C. S. Tin-coated viral nanoforests as sodium-ion battery anodes. *ACS Nano* **2013**, *7*, 3627–3634.

[34] Liang, L. Y.; Xu, Y.; Wang, C. L.; Wen, L. Y.; Fang, Y. G.; Mi, Y.; Zhou, M.; Zhao, H. P.; Lei, Y. Large-scale highly ordered Sb nanorod array anodes with high capacity and rate capability for sodium-ion batteries. *Energy Environ. Sci.* **2015**, *8*, 2954–2962.

[35] Darwiche, A.; Marino, C.; Sougrati, M. T.; Fraisse, B.; Stievano, L.; Monconduit, L. Better cycling performances of bulk Sb in Na-ion batteries compared to Li-ion systems: An unexpected electrochemical mechanism. *J. Am. Chem. Soc.* **2012**, *134*, 20805–20811.

[36] Baggetto, L.; Ganesh, P.; Sun, C. N.; Meisner, R. A.; Zawodzinski, T. A.; Veith, G. M. Intrinsic thermodynamic and kinetic properties of Sb electrodes for Li-ion and Na-ion batteries: Experiment and theory. *J. Mater. Chem. A* **2013**, *1*, 7985–7994.

[37] Baggetto, L.; Hah, H.-Y.; Jumas, J. C.; Johnson, C. E.; Johnson, J. A.; Keum, J. K.; Bridges, C. A.; Veith, G. M. The reaction mechanism of SnSb and Sb thin film anodes for Na-ion batteries studied by X-ray diffraction, ^{119}Sn and ^{121}Sb Mössbauer spectroscopies. *J. Power Sources* **2014**, *267*, 329–336.

[38] Ji, L. W.; Gu, M.; Shao, Y. Y.; Li, X. L.; Engelhard, M. H.; Arey, B. W.; Wang, W.; Nie, Z. M.; Xiao, J.; Wang, C. M. et al. Controlling SEI formation on SnSb-porous carbon nanofibers for improved Na ion storage. *Adv. Mater.* **2014**, *26*, 2901–2908.

[39] Zhou, X. L.; Zhong, Y. R.; Yang, M.; Hu, M.; Wei, J. P.; Zhou, Z. Sb nanoparticles decorated N-rich carbon nanosheets as anode materials for sodium ion batteries with superior rate capability and long cycling stability. *Chem. Commun.* **2014**, *50*, 12888–12891.

[40] Luo, B.; Wang, B.; Li, X. L.; Jia, Y. Y.; Liang, M. H.; Zhi, L. J. Graphene-confined Sn nanosheets with enhanced lithium storage capability. *Adv. Mater.* **2012**, *24*, 3538–3543.

[41] Zhu, Y. J.; Han, X. G.; Xu, Y. H.; Liu, Y. H.; Zheng, S. Y.; Xu, K.; Hu, L. B.; Wang, C. S. Electrospun Sb/C fibers for a stable and fast sodium-ion battery anode. *ACS Nano* **2013**, *7*, 6378–6386.

[42] He, C. N.; Wu, S.; Zhao, N. Q.; Shi, C. S.; Liu, E. Z.; Li, J. J. Carbon-encapsulated Fe_3O_4 nanoparticles as a high-rate lithium ion battery anode material. *ACS Nano* **2013**, *7*, 4459–4469.

[43] Jia, X. L.; Chen, Z.; Cui, X.; Peng, Y. T.; Wang, X. L.; Wang, G.; Wei, F.; Lu, Y. F. Building robust architectures of carbon and metal oxide nanocrystals toward high-performance anodes for lithium-ion batteries. *ACS Nano* **2012**, *6*, 9911–9919.

[44] Zhang, W.; Liu, Y. T.; Chen, C. J.; Li, Z.; Huang, Y. H.; Hu, X. L. Flexible and binder-free electrodes of Sb/rGO and $Na_3V_2(PO_4)_3$/rGO nanocomposites for sodium-ion batteries. *Small* **2015**, *11*, 3822–3829.

[45] Zhang, K.; Hu, Z.; Liu, X.; Tao, Z. L.; Chen, J. $FeSe_2$ microspheres as a high-performance anode material for Na-ion batteries. *Adv. Mater.* **2015**, *27*, 3305–3309.

[46] Ardizzone, S.; Fregonara, G.; Trasatti, S. "Inner" and "outer" active surface of RuO_2 electrodes. *Electrochim. Acta* **1990**, *35*, 263–267.

[47] Brezesinski, T.; Wang, J.; Tolbert, S. H.; Dunn, B. Ordered mesoporous α-MoO_3 with iso-oriented nanocrystalline walls for thin-film pseudocapacitors. *Nat. Mater.* **2010**, *9*, 146–151.

[48] Chen, Z.; Augustyn, V.; Jia, X. L.; Xiao, Q. F.; Dunn, B.; Lu, Y. F. High-performance sodium-ion pseudocapacitors based on hierarchically porous nanowire composites. *ACS Nano* **2012**, *6*, 4319–4327.

[49] Yu, D. Y. W.; Prikhodchenko, P. V.; Mason, C. W.; Batabyal, S. K.; Gun, J.; Sladkevich, S.; Medvedev, A. G.; Lev, O. High-capacity antimony sulphide nanoparticle-decorated graphene composite as anode for sodium-ion batteries. *Nat. Commun.* **2013**, *4*, 2922.

[50] Yang, Y.; Fan, X. J.; Casillas, G.; Peng, Z. W.; Ruan, G. D.; Wang, G.; Yacaman, M. J.; Tour, J. M. Three-dimensional nanoporous Fe_2O_3/Fe_3C-graphene heterogeneous thin films for lithium-ion batteries. *ACS Nano* **2014**, *8*, 3939–3946.

[51] Zhukoskii, Y. F.; Balaya, P.; Kotomin, E. A.; Maier, J. Evidence for interfacial-storage anomaly in nanocomposites for lithium batteries from first-principles simulations. Phys. *Rev. Lett.* **2006**, *96*, 058302.

[52] Jamnik, J.; Maier, J. Nanocrystallinity effects in lithium battery materials: Aspects of nano-ionics. Part IV. *Phys. Chem. Chem. Phys.* **2003**, *5*, 5215–5220.

[53] Shin, J. Y.; Samuelis, D.; Maier, J. Sustained lithium-storage performance of hierarchical, nanoporous anatase TiO_2 at high rates: Emphasis on interfacial storage phenomena. *Adv. Funct. Mater.* **2011**, *21*, 3464–3472.

[54] Balaya, P. Size effects and nanostructured materials for energy applications. *Energy Environ. Sci.* **2008**, *1*, 645–654.

[55] Nam, D. H.; Hong, K. S.; Lim, S. J.; Kim, M. J.; Kwon, H. S. High-performance Sb/Sb_2O_3 anode materials using a polypyrrole nanowire network for Na-ion batteries. *Small* **2015**, *11*, 2885–2892.